ROLE OF PLASMA EQUILIBRIUM CURRENT IN ALFVÉN WAVE ANTENNA OPTIMIZATION

Satish Puri

IPP 4/230 December 1986

MAX-PLANCK-INSTITUT FÜR PLASMAPHYSIK

8046 GARCHING BEI MÜNCHEN

MAX-PLANCK-INSTITUT FÜR PLASMAPHYSIK

GARCHING BEI MÜNCHEN

ROLE OF PLASMA EQUILIBRIUM CURRENT IN ALFVÉN WAVE ANTENNA OPTIMIZATION

Satish Puri

IPP 4/230 December 1986

Die nachstehende Arbeit wurde im Rahmen des Vertrages zwischen dem Max-Planck-Institut für Plasmaphysik und der Europäischen Atomgemeinschaft über die Zusammenarbeit auf dem Gebiete der Plasmaphysik durchgeführt.

ROLE OF PLASMA EQUILIBRIUM CURRENT IN ALFVÉN WAVE ANTENNA OPTIMIZATION

S. PURI

Max-Planck Institut für Plasmaphysik, EURATOM Association

Garching bei München, FRG

ABSTRACT

The modifications in the antenna loading produced by the plasma equilibrium current, the Faraday shield, and the finite electron temperature for coupling to the Alfvén waves are studied using a self-consistent, three-dimensional, fully analytic periodic-loop-antenna model. The only significant changes are found to occur due to the plasma current and consist of an improved coupling (by a factor of ~2.5) at low toroidal numbers ($n \sim 1-3$). Despite this gain, however, the coupling to low n continues to be poor with $R = 0.03\Omega$ and $Q = 180$ for $n = 2$. Optimum coupling with $R = 0.71\Omega$ and $Q = 16.8$ occurs for $n = 8$ as was also the case in the absence of the plasma current. For the large n values, mode splitting due to the removal of the poloidal degeneracy combined with the finite electron temperature effects lead to significant broadening of the energy absorption profile. Direct antenna coupling to the surface shear wave is small and no special provision, such as Faraday shielding, may be needed for preventing surface losses. The introduction of the Faraday screen, in fact, increases the coupling to the surface shear wave, possibly by acting as an impedance matching transformer between the antenna and the plasma. The finite electron temperature causes the predictable increase in the absorption width without influencing the antenna coupling. Thus the recommendations for antenna design for optimum coupling to the Alfvén wave remain unaffected by the inclusion of the plasma current. Efficient coupling with capabilities for dynamic impedance tracking through purely electronic means may be obtained using a dense-cluster-array antenna with a toroidal configuration of $n \sim 8$.

1. INTRODUCTION AND REVIEW OF BASIC CONCEPTS

The potential for thermonuclear plasma heating using Alfvén [1] waves was recognized in a series of articles by Winterberg [2]. Dolgopolov and Stepanov mention the possibility of electron heating via Cerenkov absorption at the Alfvén resonance [3]. These findings, however, did not become common knowledge until the independent work of Grossman and Tataronis [4] and Jankovich [5]. Hasegawa and Chen [6, 7] showed that in a hot plasma the wave conversion process plays the pivotal role of transporting the energy from the undamped fast compressional Alfvén wave (COM) to the kinetic Alfven wave (KIN), which is subsequently absorbed via electron Landau damping (ELD). The foregoing work set the stage for the considerable activity that has followed [8 – 31].

The wave dispersion relation in a slab plasma model with the inclusion of the parallel electron temperature along the magnetic field lines is given by [32],

$$An_\perp^4 - Bn_\perp^2 + C = 0 \,, \tag{1}$$

where

$$A = \epsilon_x \,, \tag{2}$$

$$B = \epsilon_x^2 - \epsilon_y^2 + \epsilon_x\epsilon_z - \epsilon_x n_z^2 - \epsilon_z n_z^2 \,, \tag{3}$$

$$C = \epsilon_z(\epsilon_L - n_z^2)(\epsilon_R - n_z^2) \,, \tag{4}$$

$$\epsilon_x = 1 - \sum_j \frac{\omega_{pj}^2}{\omega_2 - \omega_{cj}^2} \,, \tag{5}$$

$$\epsilon_y = \sum_j s_j \frac{\omega_{cj}}{\omega} \frac{\omega_{pj}^2}{\omega^2 - \omega_{cj}^2} \,, \tag{6}$$

$$\epsilon_z = 1 - \sum_j \frac{\omega_{pj}^2}{\omega^2} \zeta_j^2 Z_j'(\zeta_j) \,, \tag{7}$$

$$\epsilon_{L,R} = \epsilon_x \pm \epsilon_y \,, \tag{8}$$

$$Z_j(\zeta_j) = i\pi^{1/2} \exp(-\zeta_j^2) + \pi^{1/2} \int_{-\infty}^{\infty} \frac{\exp(-t^2)}{t - \zeta_j} dt, \; Im(\zeta_j) > 0 \,, \tag{9}$$

$$\zeta_j = \frac{c}{n_z v_t} , \tag{10}$$

$$Z_j' = \frac{\partial Z_j}{\partial \zeta_j} , \tag{11}$$

$n_\perp^2 = n_x^2 + n_y^2$, $n_\perp$ and n_z are the perpendicular and parallel refractive indices, respectively, and ϵ is the plasma dielectric tensor given by

$$\epsilon = \begin{pmatrix} \epsilon_x & -i\epsilon_y & 0 \\ i\epsilon_y & \epsilon_x & 0 \\ 0 & 0 & \epsilon_z \end{pmatrix} , \tag{12}$$

ω_p and ω_c are the plasma and the cyclotron frequencies, respectively, $Z_j(\zeta_j)$ is the plasma dispersion function [33], v_t is the particle thermal speed along the magnetic field direction, and s_j is the sign of the charge carried by the particles of type j.

Equation (1) may be factored [15] into quasi-compressional and quasi-torsional roots

$$n_\perp^2 = \epsilon_x - n_z^2 + c_1 , \tag{13}$$

and

$$n_\perp^2 = \frac{\epsilon_z}{\epsilon_x}(\epsilon_x - n_z^2) + c_2 . \tag{14}$$

The coupling terms c_1 and c_2 assume importance in the resonance region and may be obtained using (13) and (14) in (1). The qualitative dispersion curves [17] for (a) a cold plasma, (b) a hot plasma, and (c) a plasma with a monotonically increasing electron temperature profile are shown in Fig. 1. The left and the right cutoffs occur at $\epsilon_{L,R} = n_z^2$ and the position of the Alfvén layer corresponds to $\epsilon_x = n_z^2$. The dashed parts of the curves correspond to regions of significant ELD. The transition from the torsional Alfvén wave (TAW) to the kinetic Alfvén wave (KIN) is caused by the change in the sign of Z_e' (and hence of ϵ_z) as $\zeta_e \sim 1$. In the limit of vanishing electron mass both TAW and KIN collapse to form a vertical branch at the Alfvén singularity.

In most practical situations the conditions depicted in Fig. 1c prevail, with the transition from TAW to KIN lying close to the plasma edge. The azimuthally oriented antenna couples predominantly to the COM which is evanescent near the plasma edge but assumes a propagating character beyond the right cutoff. Also some of its energy

is converted to the KIN in the region of the Alfvén layer. The KIN is in turn absorbed via ELD producing plasma heating. A small additional part of the antenna energy is directly coupled to the TAW which is readily absorbed by ELD close to the plasma edge, giving rise to undesirable surface heating.

The inclusion of the plasma equilibrium current produces significant modifications by removing the poloidal degeneracy resulting in a multiplicity of resonances with their corresponding cutoffs [14, 16, 17]. Yet another important effect of the plasma current, first pointed out by the Lausanne group, is the appearance of stable kink modes. Whether the so-called discrete Alfvén waves (DAW) can be usefully exploited for plasma heating continues to be a controversial issue [19, 20, 22, 24].

The COM is weakly [15] damped with a radial damping length of several thousand kilometers. The KIN, however, is readily absorbed via ELD with the radial damping length given by

$$k_{xi}^{-1} \approx \frac{1}{\sqrt{2\pi}} \frac{c}{\omega_{pe}} \frac{exp(\zeta_e^2)}{\zeta_e^2} \ , \tag{15}$$

which is typically of the order of a few centimeters [15]. The vastly different wavelengths of COM and KIN, the strong evanescence effects as well as the rapid increase in the TAW refractive index near the plasma edge, contribute to the difficulties in an accurate integration of the Maxwell's equations. Ross, Chen and Mahajan [17] have conducted a boundary value analysis in a model that incorporates the COM, the TAW, the KIN, the plasma current and even the finite Larmor radius effects. The difficult integrations are tackled in an elegant manner by employing a Galerkin procedure with cubic spline elements.

Modifications in the Alfvén wave propagation characteristics are also predicted due to the poloidal mode coupling by the inclusion of toroidicity [14, 16, 25, 29]. The precise quantitative estimate of the fraction of the antenna energy diverted to the parasitic modes is, however, not presently available; extensive global mode studies in toroidal geometries are being pursued.

The wave conversion process from the COM to the KIN in the plasma interior is

critical to the Alfvén wave heating scheme [6]. For finite n_y, $n_x^2 = n_\perp^2 - n_y^2$ may be obtained by displacing the abscissa in Fig. 1 by n_y^2 so that the right cutoff moves further away from the resonance region thereby decreasing the coupling to the fast wave. This apparently causes the well-known increase in the wave conversion to the slow branch resulting in the superior coupling at the $|m| = 1$ azimuthal modes. Still larger values of $|m|$, however, cause a reduction in coupling due to the increased evanescence. An improvement in the conversion efficiency also accompanies an increase in the ω/ω_{ci} ratio and hence upon the toroidal wave number n [14 – 17]. Two basic effects of increasing n (and concomitantly the frequency) are (i) to increase the separation between the resonance and the cutoffs, and (ii) to provide a larger effective distance (measured in wavelengths) for wave conversion due to the reduced wavelength at the higher frequency of operation. Both these effects contribute to an increased coupling to KIN. An approximate analytical derivation of this effect is given in the Appendix. Too large a value of n, however would cause diminished coupling owing to the field cancellation effects from the adjacent antenna sections [14 – 17].

Important progress has been made in the experimental documentation of the basic physics of Alfvén wave heating especially by the Austin [17] and the Lausanne [18, 25, 30] groups. In addition to the antenna loading characteristics, direct observation of the wave conversion, as well as effects associated with the plasma current and toroidicity have been recorded.

Efficient coupling to the Alfvén waves requires (i) conditions conducive to high conversion efficiency, and (ii) minimization of the evanescence between the plasma edge and the singular surface. These happen to be contradictory requirements. The first of these conditions demands the choice of a large ω/ω_{ci} ratio (requiring a high toroidal number n and hence a densely packed longitudinal antenna configuration), whereas the second condition is best satisfied at low frequencies and therefore for low values of n. Although this predicament has been recogonized previously, the precise quantitative implications were brought to a focus in our recent antenna optimization study [31]. It was shown

that optimal coupling, possessing high efficiency and low Q necessary for thermonuclear applications, would not be feasible with the low toroidal number (e.g., $n \sim 2$) antennas employed in the current experimental practice. Acceptable coupling may require using $n \sim 8$. The antenna structure will take the form of a dense cluster of limited longitudinal extent, reminiscent of the grill coupler used for the lower hybrid heating. Unlike the grill antenna which is used to provide accessibility, the cluster antenna promotes higher conversion efficiency. The penalty for using such large toroidal wave numbers is the strong radial evanescence suffered by the wave. Thus the resonant layer has to be located approximately at two-thirds the plasma radius (roughly corresponding to the center of the plasma volume). This may constitute a viable choice for heating the entire plasma volume, particularly if the energy distribution is aided by the enhanced electron heat conduction.

The results of Ref. [31] were obtained without the inclusion of the plasma equilibrium current which has an important bearing upon the Alfvén wave characteristics for the low $|n/m|$ values. The role of the plasma current in the antenna optimization is addressed in this paper. Allowing for the possibility of the TAW wave excitation due to the finite angle of the magnetic field lines with the cylindrical axis, requires the inclusion of finite electron temperature as well. Finally, a more flexible version of the Faraday screen with the capability of variable inclination with respect to the magnetic field direction has been incorporated in order to enable us to suppress any offending surface heating effects.

Allowing for an inclination σ in the Faraday shield with respect to the *local* direction of the magnetic field lines requires the following modifications in the tensor components M_{i3} and N_{3j} of Ref. [34]

$$M_{i3} = [(\alpha_1 S_\sigma + \alpha_2 C_\sigma)\epsilon(c+f),\ (\alpha_2 S_\sigma + \alpha_3 C_\sigma)\epsilon(c+f),$$
$$(\alpha_1 S_\sigma^2 + 2\alpha_2 C_\sigma S_\sigma + \alpha_3 C_\sigma^2 - \varsigma_F),$$
$$(\alpha_1 S_\sigma + \alpha_2 C_\sigma)\epsilon(a-f),\ (\alpha_2 S_\sigma + \alpha_3 C_\sigma)\epsilon(a-f)]\ , \tag{16}$$

and

$$N_{3j} = [.5(n_y S_\sigma + n_z C_\sigma)u_{x-f},\ (\alpha_1 S_\sigma + \alpha_2 C_\sigma),\ (\alpha_2 S_\sigma + \alpha_3 C_\sigma),$$

$$(\alpha_5 S_\sigma + \alpha_4 C_\sigma),\ .5 C_\sigma u_{x-f}, -.5 S_\sigma u_{x-f}] \ , \tag{17}$$

where, $C_\sigma = \cos\sigma$, $S_\sigma = \sin\sigma$, while α_k, ς_F, $\epsilon(x)$, and u_x remain as defined in Ref. [34].

The single antenna geometry of Ref. [34] and the fully analytic antenna treatment developed in Ref. [31] will be used. As in Ref. [30], m and n denote the poloidal and the toroidal wave numbers while M and N pertain to the antenna geometry. Thus $M \equiv 1$ azimuthal antenna configuration used throughout the computations denotes a single antenna elememt in the poloidal direction. Assuming that the alternate antenna sections along the toroidal direction are in phase opposition, $N = N_A/2$, where N_A is the number of antenna sections deployed along the toroidal circumference.

2. THE PLASMA DESCRIPTION AND THE LOCAL COORDINATES

The density and electron temperature are assumed to vary as

$$\frac{n_e}{n_e(0)} = \left[1 - \left(\frac{r}{r_{0n}}\right)^{\chi_n}\right] \exp\left[-\frac{1}{2}\left(\frac{r}{r_{\sigma n}}\right)^2\right] , \tag{18}$$

and

$$\frac{T_e}{T_e(0)} = \left[1 - \left(\frac{r}{r_{0t}}\right)^{\chi_t}\right] \exp\left[-\frac{1}{2}\left(\frac{r}{r_{\sigma t}}\right)^2\right] , \tag{19}$$

where χ and r_σ are the profile weight and the variance of the Gaussian, respectively. The quantities r_{0n} and r_{0t} are determined by the edge density $n_e(r_p)$ and edge temperature $T_e(r_p)$ in the following manner

$$\frac{r_{0n}}{r_p} = \left[\left\{1 - \frac{n_e(r_p)}{n_e(0)}\right\} \exp\left\{\frac{1}{2}\left(\frac{r_p}{r_{\sigma n}}\right)^2\right\}\right]^{-1/\chi_n} , \tag{20}$$

and

$$\frac{r_{0t}}{r_p} = \left[\left\{1 - \frac{T_e(r_p)}{T_e(0)}\right\} \exp\left\{\frac{1}{2}\left(\frac{r_p}{r_{\sigma t}}\right)^2\right\}\right]^{-1/\chi_t} , \tag{21}$$

where r_p is the plasma radius.

Although the present treatment is limited to cylindrical plasmas, it is convenient to introduce the effect of the plasma current through the safety factor q given by

$$q = q_{max} - (q_{max} - q_{min}) \left[1 - \left(\frac{r}{r_p}\right)^{\chi_q}\right] \exp\left[-\frac{1}{2}\left(\frac{r}{r_{\sigma q}}\right)^2\right] , \tag{22}$$

where, $q_{max} = q(r_p)$ and $q_{min} = q(0)$. From q, one obtains the angle χ between the z-axis and the magnetic field lines using

$$\chi = \arctan(\frac{r}{qr_T}) , \tag{23}$$

where r_T is the toroidal radius. The local coordinates are related to the cylindrical coordinates by the relations

$$\hat{\xi} = \hat{r} , \tag{24}$$

$$\hat{\eta} = C\hat{\theta} - S\hat{z} , \tag{25}$$

and

$$\hat{\varsigma} = S\hat{\theta} + C\hat{z} , \tag{26}$$

where $C = \cos\chi$, $S = \sin\chi$, and the hat represents a unit vector. The refractive index components in the local coordinates become

$$n_\eta = Cn_\theta - Sn_z , \tag{27}$$

and

$$n_\varsigma = Sn_\theta + Cn_z = Cn_z\left(1 + \frac{m}{nq}\right) , \tag{28}$$

where, $n_\theta = m/r$ and $n_z = n/r_T$. The Alfvén resonance relation

$$\epsilon_\xi = n_\varsigma^2 = C^2 n_z^2 \left(1 + \frac{m}{nq}\right)^2 , \tag{29}$$

involves both m and n because of the removal of the poloidal degeneracy [14, 17]. For low toroidal numbers n, the dominant antenna coupling takes place to the $m = -n/|n|$ poloidal wave number as it occurs closer to the plasma edge than its counterpart, the $m = +n/|n|$ mode. This distinction, however, disappears for larger values of n. In

the computed results reported here, the radial position of the dominant poloidal mode ($m = -n/|n|$) was kept fixed as other plasma and antenna parameters were varied in order to be able to distinguish among the effects of various parameters on the antenna loading. The local cyclotron frequency increases by the factor sec χ owing to the presence of the plasma current. The vector operations in the local coordinate system are given by

$$\nabla\phi = \frac{\partial\phi}{\partial r}\hat{\xi} + in_\eta\phi\hat{\eta} + in_\varsigma\phi\hat{\varsigma} \ , \tag{30}$$

$$\nabla\cdot\mathbf{A} = \frac{1}{r}\frac{\partial}{\partial r}(rA_\xi) + in_\eta A_\eta + in_\varsigma A_\varsigma \ , \tag{31}$$

and

$$\nabla\times\mathbf{A} = i(-n_\varsigma A_\eta + n_\eta A_\varsigma)\hat{\xi} + (in_\varsigma A_\xi + \chi'_m A_\eta - \frac{S^2}{r}A_\varsigma - A'_\varsigma)\hat{\eta}$$

$$+(-in_\eta A_\xi + \frac{C^2}{r}A_\eta + A'_\eta + \chi'_p A_\varsigma)\hat{\varsigma} \ , \tag{32}$$

where the prime denotes derivative with respect to r, and

$$\chi'_{p,m} = \chi' \pm \frac{CS}{r} \ . \tag{33}$$

3. THE VARIATIONAL FORMULATION

From the Maxwell's equations

$$\nabla\times\mathbf{E} = i\mathbf{H} \ , \tag{34}$$

and

$$\nabla\times\mathbf{H} = -i\epsilon\cdot\mathbf{E} + \mathbf{J} \ , \tag{35}$$

one obtains

$$\mathbf{E} = i(\kappa\cdot\nabla\times\mathbf{H} - \kappa\cdot\mathbf{J}) \ , \tag{36}$$

where ϵ is the dielectric tensor in the local coordinates, $\mathbf{J}$ is the radiofrequency current (applied or induced) in the various conductors,

$$\kappa = \epsilon^{-1} = \begin{pmatrix} \kappa_\xi & i\kappa_\eta & 0 \\ -i\kappa_\eta & \kappa_\xi & 0 \\ 0 & 0 & \kappa_\varsigma \end{pmatrix} , \tag{37}$$

$$\kappa_\xi = \frac{\epsilon_\xi}{\epsilon_\perp^2} , \tag{38}$$

$$\kappa_\eta = \frac{\epsilon_\eta}{\epsilon_\perp^2} , \tag{39}$$

$$\kappa_\varsigma = \frac{1}{\epsilon_\varsigma} , \tag{40}$$

and

$$\epsilon_\perp^2 = \epsilon_\xi^2 - \epsilon_\eta^2 . \tag{41}$$

Multiplying both sides of (36) by $\nabla \times \tilde{\mathbf{H}}^*$ gives

$$\nabla \cdot (\mathbf{E} \times \tilde{\mathbf{H}}^*) = i \left[\mathbf{H} \cdot \tilde{\mathbf{H}}^* - (\kappa \cdot \nabla \times \mathbf{H}) \cdot (\nabla \times \tilde{\mathbf{H}}^*) + (\kappa \cdot \mathbf{J}) \cdot (\nabla \times \tilde{\mathbf{H}}^*) \right] . \tag{42}$$

Integrating over the plasma volume yields the variational form

$$\int_S (\mathbf{E} \times \tilde{\mathbf{H}}^*) \cdot dS = i \int_V \left[\mathbf{H} \cdot \tilde{\mathbf{H}}^* - (\kappa \cdot \nabla \times \mathbf{H}) \cdot (\nabla \times \tilde{\mathbf{H}}^*) + (\kappa \cdot \mathbf{J}) \cdot (\nabla \times \tilde{\mathbf{H}}^*) \right] dV. \tag{43}$$

The electric field $\mathbf{E}$ on the left hand side of (43) is to be prescribed by the boundary conditions, consisting of either the driving source terms at the surface (Section 5) or regularity conditions at the axis (Section 4). The sole restriction on $\tilde{\mathbf{H}}$ is that it should satisfy the boundary conditions imposed on $\mathbf{H}$. The casting of the variational equation in terms of $\mathbf{H}$ instead of the usual $\mathbf{E}$ may be computationally advantageous because compared to their electric field counterparts, the magnetic field components exhibit considerably more placid behavior.

Equation (43) has been integrated to solve for the plasma surface impedance tensor ς_P by standard finite element techniques [35] employing cubic Hermite interpolation elements. Details of these computations will be given in a separate communication.

If $\tilde{\mathbf{H}} = \mathbf{H}$, (42) corresponds to twice the dissipation density. Similarly (36) may be used to obtain the Poynting vector $\mathbf{P}$. Also

$$\bar{\mathbf{P}} = 2\pi r \frac{\pi r_T}{N} \mathbf{P} , \tag{44}$$

is the total Poynting vector per antenna, while

$$\nabla \cdot \bar{\mathbf{P}} = 2\pi r \frac{\pi r_T}{N} \nabla \cdot \mathbf{P} , \tag{45}$$

gives the dissipation per unit radial distance per antenna.

4. REGULARITY CONDITIONS AT THE AXIS

Upon eliminating E_ξ and H_ξ, the Maxwell's equations may be expressed in the form

$$E'_\eta = -(\frac{C^2}{r} + \frac{n_\eta \epsilon_\eta}{\epsilon_\xi})E_\eta - \chi'_p E_\varsigma + i\frac{n_\eta n_\varsigma}{\epsilon_\xi}H_\eta + i(1 - \frac{n_\eta^2}{\epsilon_\xi})H_\varsigma \ , \tag{46}$$

$$E'_\varsigma = (\chi'_m - \frac{n_\varsigma \epsilon_\eta}{\epsilon_\xi})E_\eta - \frac{S^2}{r}E_\varsigma - i\frac{\gamma_1}{\epsilon_\xi}H_\eta - i\frac{n_\eta n_\varsigma}{\epsilon_\xi}H_\varsigma \ , \tag{47}$$

$$H'_\eta = -in_\eta n_\varsigma E_\eta + i(n_\eta^2 - \epsilon_\varsigma)E_\varsigma - \frac{C^2}{r}H_\eta - \chi'_p H_\varsigma \ , \tag{48}$$

and

$$H'_\varsigma = i(\gamma_1 - \frac{\epsilon_\eta^2}{\epsilon_\xi})E_\eta + in_\eta n_\varsigma E_\varsigma + (\chi'_m - \frac{n_\varsigma \epsilon_\eta}{\epsilon_\xi})H_\eta + (\frac{n_\eta \epsilon_\eta}{\epsilon_\xi} - \frac{S^2}{r})H_\varsigma \ , \tag{49}$$

where,

$$\gamma_1 = \epsilon_\xi - n_\varsigma^2 \ . \tag{50}$$

At the axis for $r \to 0$, $\chi \to 0$, $S \to 0$ and $C \to 1$.

4.1 Polarization relations for the $m = 0$ case

Since $n_\eta \to 0$, assuming that the plasma parameters are slowly varying near the axis, (46) to (49) simplify to

$$(rE_\eta)' = irH_\varsigma \ , \tag{51}$$

$$E'_\varsigma = -\frac{n_\varsigma \epsilon_\eta}{\epsilon_\xi}E_\eta - i\frac{\gamma_1}{\epsilon_\xi}H_\eta \ , \tag{52}$$

$$(rH_\eta)' = -ir\epsilon_\varsigma E_\varsigma \ , \tag{53}$$

and

$$H'_\varsigma = i(\gamma_1 - \frac{\epsilon_\eta^2}{\epsilon_\xi})E_\eta - \frac{n_\varsigma \epsilon_\eta}{\epsilon_\xi}H_\eta \ . \tag{54}$$

For the polarization corresponding to $H_\varsigma \equiv 0$, (51) shows that $E_\eta \to 0$. From (52) to (54), one obtains

$$E''_\varsigma + \frac{1}{r}E'_\varsigma + \kappa_1^2 E_\varsigma = 0 \ , \tag{55}$$

where

$$\kappa_1^2 = \frac{\gamma_1 \epsilon_\varsigma}{\epsilon_\xi} \ . \tag{56}$$

From (55) and (52) we get the polarization relations for $r \to 0$ as

$$E_\varsigma = J_0(\kappa_1 r) \ , \tag{57}$$

and

$$H_\eta = -i \left(\frac{\epsilon_\xi \epsilon_\varsigma}{\gamma_1} \right)^{1/2} J_1(\kappa_1 r) \ , \tag{58}$$

where J_n are the Bessel functions of the first kind and order n.

Similarly for the wave polarization $E_\varsigma \equiv 0$, $H_\eta \to 0$,

$$E_\eta = i \frac{J_1(\kappa_2 r)}{\kappa_2} \ , \tag{59}$$

and

$$H_\varsigma = J_0(\kappa_2 r) \ , \tag{60}$$

where

$$\kappa_2^2 = \gamma_1 - \frac{\epsilon_\eta^2}{\epsilon_\xi} \ . \tag{61}$$

4.2 Polarization relations for the $m \neq 0$ case

At the axis we assume that the field components vary as

$$\{ r E_\eta, E_\varsigma, r H_\eta, H_\varsigma \} \sim r^{\beta_{1,2}} \ . \tag{62}$$

Using (62) in (46) to (49) gives

$$\beta_{1,2}^2 = m^2, \left(m^2 - \frac{\gamma_1 \epsilon_\varsigma}{\epsilon_\xi} r^2 \right) \ . \tag{63}$$

Together with (46) to (48), (63) provides the polarization relations

$$E_\eta = -i \frac{m^2}{\epsilon_\xi} (\beta_{1,2}^2 - m^2 + \epsilon_\varsigma r^2) \ , \tag{64}$$

$$E_\varsigma = i\frac{mn_\varsigma}{\epsilon_\xi}(m^2 - \beta_{1,2}^2)r \ , \tag{65}$$

$$H_\eta = -\frac{n_\varsigma \epsilon_\varsigma}{\epsilon_\xi}\beta_{1,2} m r^2 \ , \tag{66}$$

and

$$H_\varsigma = (\beta_{1,2}^2 - m^2)\left(\beta_{1,2} + \frac{m\epsilon_\eta}{\epsilon_\xi}\right) r + \frac{\epsilon_\varsigma}{\epsilon_\xi}(\beta_{1,2}\gamma_1 - m\epsilon_\eta) r^3 \ . \tag{67}$$

Two independent sets of polarizations correspond to the two values of $\beta_{1,2}$ in (63).

4.3 The regularity conditions for $r \to 0$

For $r \to 0$, let $p(r)$ and $q(r)$ be the amplitudes of the two waves corresponding respectively to the two wave polarizations. The total field in the plasma may be expressed as the superposition of these two components

$$E_\eta(r) = p(r)E_\eta^p(r) + q(r)E_\eta^q(r) \ , \tag{68}$$

$$E_\varsigma(r) = p(r)E_\varsigma^p(r) + q(r)E_\varsigma^q(r) \ , \tag{69}$$

$$H_\eta(r) = p(r)H_\eta^p(r) + q(r)H_\eta^q(r) \ , \tag{70}$$

and

$$H_\varsigma(r) = p(r)H_\varsigma^p(r) + q(r)H_\varsigma^q(r) \ . \tag{71}$$

Eliminating $p(r)$ and $q(r)$, gives

$$E_\eta(r) = z_{11}(r)H_\eta(r) + z_{12}(r)H_\varsigma(r) \ , \tag{72}$$

and

$$E_\varsigma(r) = z_{21}(r)H_\eta(r) + z_{22}(r)H_\varsigma(r) \ , \tag{73}$$

where

$$z_{11} = (E_\eta^p H_\varsigma^q - E_\eta^q H_\varsigma^p)D^{-1} \ , \tag{74}$$

$$z_{12} = (E_\eta^q H_\eta^p - E_\eta^p H_\eta^q)D^{-1} \ , \tag{75}$$

$$z_{21} = (E_\varsigma^p H_\varsigma^q - E_\varsigma^q H_\varsigma^p)D^{-1} \ , \tag{76}$$

$$z_{22} = (E_\varsigma^q H_\eta^p - E_\varsigma^p H_\eta^q) D^{-1} \ , \tag{77}$$

and

$$D = H_\eta^p H_\varsigma^q - H_\eta^q H_\varsigma^p \ . \tag{78}$$

Equations (72) and (73) along with (74) to (77) completely specify the regularity conditions at the axis. The expressions (72) and (73) for E_η and E_ς, respectively, help to eliminate $\mathbf{E}$ in the left hand side of the variational form (43).

5. BOUNDARY CONDITIONS AT THE PLASMA SURFACE

At $r = r_p$, the surface magnetic field may be related to the surface electric field through the admittance matrix $\boldsymbol{\Upsilon}_P$ by the following expressions

$$H_\eta(r_p) = \Upsilon_{11} E_\eta(r_p) + \Upsilon_{12} E_\varsigma(r_p) \ , \tag{79}$$

and

$$H_\varsigma(r_p) = \Upsilon_{21} E_\eta(r_p) + \Upsilon_{22} E_\varsigma(r_p) \ . \tag{80}$$

Imposing the boundary conditions $E_\eta(r_p) = 1$ and $E_\varsigma(r_p) = 0$ at once eliminates $\mathbf{E}$ in (43). The solution matrix directly yields $\Upsilon_{11} = H_\eta(r_p)$ and $\Upsilon_{21} = H_\varsigma(r_p)$. Repeating the procedure with $E_\eta(r_p) = 0$ and $E_\varsigma(r_p) = 1$ gives the remaining two components of the admittance matrix at the plasma surface.

The plasma surface impedance matrix $\boldsymbol{\varsigma}_P$ may now be obtained from the relations

$$\varsigma_{11} = \Upsilon_{22} \Delta^{-1} \ , \tag{81}$$

$$\varsigma_{12} = -\Upsilon_{12} \Delta^{-1} \ , \tag{82}$$

$$\varsigma_{21} = -\Upsilon_{21} \Delta^{-1} \ , \tag{83}$$

$$\varsigma_{22} = \Upsilon_{11} \Delta^{-1} \ , \tag{84}$$

where

$$\Delta = \Upsilon_{11} \Upsilon_{22} - \Upsilon_{12} \Upsilon_{21} \ . \tag{85}$$

The ς_P thus obtained is employed in the antenna calculations described in Refs. [31,34].

6. THE RESULTS

The ASDEX UPGRADE parameters used in the computations described in this section are listed in TABLE I. The dot on the abscissa of the following figures corresponds to these reference parameters. The antenna efficiency η_A is defined as the ratio of the net power delivered into the plasma versus the power entering the antenna terminals. The antenna dissipation accounts for over ninety percent of the total resistive losses in the system, the rest occuring in the wall and the Faraday shield. Unless explicitly stated, the metallic surfaces are assumed to be silver plated and the Faraday screen is not included. The quality factor is defined as $Q = |X|/R$, where X and R, respectively, are the inductive and the resistive components of the antenna impedance Z_A. The position r_A of the singular Alfvén surface corresponding to the $m = -n/|n|$ resonance is treated as the primary fixed parameter. In order to maintain r_A constant, the frequency of operation is varied in accordance with the plasma and the antenna conditions. The total number of antenna sections along one torus circumference $N_A = 2N$. The alternate sections are assumed to be in phase opposition so that the fundamental toroidal wave number $n = N$. Each antenna section is composed of a single element presumed to be placed along the outer plasma circumference. The toroidal geometry is simulated by the cylindrical approximation via the periodicity in the z direction. Although the plasma surface impedance is computed using the cylindrical model, the antenna computations employ the fully analytic, self-consistent slab treatment of Refs. [31,34]. The use of slab antenna model is justified because of the relatively short separation between the antenna and the plasma surface, so that the cylindrical effects are negligible.

Figure 2 depicts the dependence of antenna loading on N. The inclusion of the plasma equilibrium current produces no significant alteration in the basic result of Ref. [31]. As before an antenna configuration with $N \sim 8$ is imperative for good coupling. The significance of the quality factor Q may be appreciated from the circuit theory

definitions (for input power P_A and assuming $Q \gg 1$)

$$V \approx (P_A Q X)^{1/2} , \tag{86}$$

$$I \approx (P_A \frac{Q}{X})^{1/2} , \tag{87}$$

and

$$VI \approx P_A Q . \tag{88}$$

Figure 3 showing the antenna voltage and current characteristics as a function of N, conveys the practical implication of these results. For 1 MW power input per antenna, the $N = 2$ antenna requires 31 kV and 5.8 kA contrasted with the 14 kV and 1.2 kA needed for the $N = 8$ antenna (assuming $r_A/r_p = .67$). Even after allowing for some relief in the voltage requirements by employing antennas with a larger width, the problems with the low N antennas remain formidable.

The cooling problems too become severe for the low N antennas (Fig. 4), 13% of the input power being dissipated in the antenna itself for the $N = 2$ configuration, compared to the more tolerable loss of 1.2% for the $N = 8$ antenna. If instead of silver, stainless steel were to be used as the antenna material, the corresponding losses rise to 48% and 6.6%, respectively. For appreciably smaller values of r_A/r_p, even the operation at $N = 8$ may be jeopardized.

The precise effect of the equilibrium current is seen in Figs. 5 and 6 for the two antenna configurations $N = 2$ and $N = 8$, respectively. The effect of the plasma current is simulated by varying the safety factor q_{min} at the axis while keeping $q_{max}/q_{min} = 3$. For the $N = 2$ case, the coupling to the $m = -1$ resonance clearly dominates over the $m = +1$ contribution. Although there is distinct improvement in antenna loading for increasing plasma current, the coupling for the low N values continues to be poor. The improvement in antenna loading with increasing plasma current is in agreement with the theoretical as well as the experimental results reported in Ref. [30].

The decline in antenna loading for decreasing r_A/r_p is shown in Figs. 7 and 8. The sharper reduction for the $N = 8$ case is to be traced to the stronger evanescence due

to the close juxtapostion of the antenna sections. The reduction in loading when the resonance occurs too close to the plasma edge does not have a counterpart in the absence of the plasma current.

Figures 9 and 10 are the plots of $-\bar{P}_\xi$ and $(\nabla \cdot \bar{\mathbf{P}})_m$ depicting the Poynting vector per antenna and the azimuthal components of the dissipation (per antenna) per unit radial distance for $T_e = 1\ keV$ and $T_e = 10\ keV$, respectively. The fraction of the wave energy already absorbed is indicated by the dots on the $-\bar{P}_\xi$ curve. Combination of the finite electron temperature and the mode separation due to the removal of the azimuthal degeneracy results in considerable broadening of the dissipation profile for the large N values because the dominant pair of the $m = \pm 1$ modes are excited with comparable strength. This advantage will not accompany the low N excitation because of the relatively weak excitation of the $m = +1$ azimuthal mode.

The radiofrequency magnetic field in the plasma for the parameters of TABLE I is plotted in Fig. 11. The wave conversions near the resonances require the existence of a Poynting vector associated with KIN in order to carry off the wave converted energy from COM. Since the E_ζ component of the electric field is vanishingly small, H_η exhibits large excursions near the resonance in order to provide for the energy transport to KIN. Figure 12 depicts the components of the displacement vector $\mathbf{D} = \epsilon \cdot \mathbf{E}$. The component D_η increases as a resonance is approached, followed by an equally rapid restoration as the enegy is drawn away from the fast COM to feed the KIN. As a result, the D_ζ component grows, but it, too, quickly subsides as it encounters strong Landau damping. The D_ξ field mimics the D_ζ fluctuations in order to satisfy the continuity requirement $\nabla \cdot \mathbf{D} = 0$. The behavior of $\mathbf{E}$ (Fig. 13) follows that of $\mathbf{D}$. The component E_ζ, being several orders of magnitude smaller than the other two components, is not shown.

The small blip in D_ζ in Fig. 12 is due to the direct excitation of the TAW near the plasma edge. The associated electric field E_ζ is extremely small. Furthermore, since there is no concomitant increase in H_η, the enregy diverted to the edge heating is small (estimated to be below 0.2%). The prevailing absence of the edge heating has been a

consistently welcome feature throughout the computations. Ironically enough, the edge heating flares up in a significant manner upon the introduction of the Faraday screen, unless care is exercised in the alignment with respect to the magnetic field lines. Figure 14 shows the fraction of the antenna energy coupled to the surface wave as a function of the angle $(\sigma - \chi)°$, which is a measure of the Faraday shield misalignment with respect to the magnetic field lines.

7. DISCUSSION

7.1 Optimal coupling configuration

The primary objective of this work has been to explore the existence of windows in the parameter space conducive for coupling to the Alfvén resonance in the presence of the equilibrium plasma current. The principal conclusion to emerge from the present investigation is that the use of high ($n \sim 8$) toroidal wave numbers is imperative for obtaining acceptable coupling in the context pertinent to thermonuclear plasma heating. Assuming an antenna configuration of $N = 8$, a further constraint consists of locating the resonance at approximately two-thirds the plasma radius, which corresponds to depositing the wave energy into the longitudinal motion of the electrons via Landau damping roughly at the center of the plasma volume. Neither of these basic constraints is significantly altered by the inclusion of the plasma equilibrium current which affects coupling mainly at low n values which are, in any case, unsuited for thermonuclear applications. These traits have been highlighted in practical terms through the presentation of antenna voltage and current as well as the resistive losses.

7.2 Surface losses due to the direct excitation of the torsional Alfvén wave

Among the more welcome findings has been the absence of serious surface heating effects which could undermine an otherwise tenable scheme. These findings are in

agreement with the TCA [30] results where the contribution to the antenna loading due to the direct parasitic loading from the TAW is estimated to be below 5 $m\Omega$. The low coupling to the surface mode may be indicative of the degree of mismatch between the antenna impedance and the effectual short circuit existing along the magnetic field lines at the relatively low frequencies encountered in the Alfvén wave heating. Strangely enough, the introduction of the Faraday screen enhances coupling to the surface wave. This behavior may possibly arise from the Faraday shield aligned along the magnetic field lines acting as an impedance matching transformer between the azimuthal antenna and the longitudinally conducting plasma. It is apparently preferable to discard the Faraday shield altogether. If the need for a particle screen to avoid breakdown problems is deemed necessary, either careful alignment, or perhaps the usage of a non conducting material, is called for.

7.3 Discrete Alfvén wave (DAW) excitation

No deliberate attempt either to include or to exclude the DAW resonances was made during the course of these computations. Nevertheless, over the broad range of parameters studied, no evidence of pronounced irregularities in the antenna loading characteristics were observed. These results indicate that an inadvertent excitation of DAW, attended by uncertain consequences, constitutes no particular cause for concern.

7.4 The computational accuracy

The variational formulation in Section 3 anticipated a more regular behavior by the magnetic field components in comparison with the electric field counterpart in the plasma. This is clearly demonstrated in Figs. 11 to 13 where the magnetic field components differ by a factor of approximately thirty, whereas the electric field components differ by several orders of magnitude. An intermediate variation is exhibited by the components of the displacememnt vector.

Figure 15 shows the convergence in the value of the antenna loading as the number of grid points in the finite element integration scheme is increased. Convergence within 0.2% of the final value occurs for surprisingly coarse grids with points a centimeter apart. This is partly a tribute to the excellent interpolation properties of the Hermite cubics between the grid points, so that the wave conversion from COM to KIN is accurately rendered even though the grid points are not closely packed around the resonance. Partly, however, the remarkable convergence is due to the insensitivity of the KIN to the precise description of the absorption process. The computations reported in this paper were performed with 750 grid points.

Notwithstanding the excellent convergence of the antenna loading, inaccuracy persists in estimating the precise amount of energy coupled to the surface wave. The underlying reasons include (i) the extreme variations in the refractive index of the slow wave in the vicinity of the plasma boundary, (ii) the interference among the modes, and (iii) the smallness of the coupled energy, *per se*. We are exploring means of improving the accuracy near the edge. Meanwhile, the estimates given for the edge heating in this paper may be subject to modification.

The insensitivity of the wave conversion and absorption to the precision in the description of KIN, together with the insignificant importance of the cyclotron damping justifies the neglect of the finite Larmor radius effects in this paper.

ACKNOWLEDGMENTS

I am thankful to Herr T. Krücken and Dr. M. Brambilla for introducing me to the finite element analysis.

Appendix

The approximate differential equation for the fast wave in the slab plasma model is given by [36] (x is not normalized in this section)

$$\mathcal{E}_y'' - k_x^2(x)\mathcal{E}_y = 0 \ , \tag{A1}$$

where

$$E_y = (\frac{\gamma_2}{\gamma_1})^{1/2}\mathcal{E}_y \ , \tag{A2}$$

$$\gamma_2 = \gamma_1 - n_y^2 \ , \tag{A3}$$

$$k_x^2(x) = \frac{(\epsilon_L - n_z^2)(\epsilon_R - n_z^2)}{\epsilon_x - n_z^2}k_0^2 - k_y^2 - k_g^2 \ , \tag{A4}$$

and

$$k_g^2(x) = \frac{n_y^2}{\gamma_1\gamma_2}\left[.5\epsilon_x'' - \frac{\epsilon_x - .25n_y^2 - n_z^2}{\gamma_1\gamma_2}\epsilon_x'^2 - \frac{\epsilon_y}{n_y}k_0\epsilon_x' + \frac{\gamma_2}{n_y}k_0\epsilon_y'\right] \ . \tag{A5}$$

The three terms in the brackets in (A5) are the contributions from the uniform plasma, the finite k_y, and the gradient effects, respectively. The presence of the k_y^2 term has the effect of translating the abscissa in Fig. 1, moving the right cutoff away from the resonance region, and thereby diminishing the coupling to the propagating branch of COM. Less important modifications are contributed by the gradient term. For a linear density profile one may approximately refactor (A4) into the form

$$k_x^2(x) = k_0^2(n_z^2 - 1)\frac{x_0}{x_{c1}x_{c2}}\frac{(x - x_{c1})(x - x_{c2})}{x - x_0} \ , \tag{A6}$$

where x_{c1} and x_{c2} correspond to the zeros of (A4). For the large $k_y^2 \sim r_p^{-2}$ encountered in the $m \neq 0$ case, the cutoff at x_{c2} is well removed from the resonance region so that

$$k_x^2(x) \approx -\alpha k_0^2\frac{x - x_{c1}}{x - x_0} \ , \tag{A7}$$

where

$$\alpha = (n_z^2 - 1)\frac{x_0}{x_{c1}} \ . \tag{A8}$$

Using (A7) reduces (A1) to the Whittaker equation

$$\frac{\partial^2\mathcal{E}}{\partial\gamma^2} + k_0^2(-\frac{1}{4} - \frac{1}{2}\frac{\beta}{\gamma})\mathcal{E} = 0 \ , \tag{A9}$$

where

$$\beta = \alpha^{1/2} k_0 (x_0 - x_{c1}) \ , \tag{A10}$$

and

$$\gamma = 2\alpha^{1/2} k_0 (x - x_0) \ . \tag{A11}$$

Discarding growing solutions, one obtains from (A9) and (A2)

$$E_y = (\frac{\gamma_2}{\gamma_1})^{1/2} \ W_{\kappa,\mu}(\gamma) \ , \tag{A12}$$

where $W_{\kappa,\mu}(\gamma)$ is the Whittaker function as given in Ref. [37], $\mu = 1/2$ and $\kappa = -\beta/2$. Using the relations

$$H_z = -i\frac{\gamma_1}{\gamma_2}\frac{\partial E_y}{\partial x} \ , \tag{A13}$$

and

$$\varsigma_f = \frac{E_y(0)}{H_z(0)} \ , \tag{A14}$$

yields

$$\varsigma_f = ik_0 x_0 \frac{n_y^2 + n_z^2 - 1}{n_z^2 - 1}\left[\frac{.5n_y^2}{n_y^2 + n_z^2 - 1} + .5\alpha^{1/2} k_0 (x_0 + x_{c1}) + \frac{U(.5\beta, 2, \gamma)}{U(1 + .5\beta, 2, \gamma)}\right]^{-1} \ , \tag{A15}$$

where $U(a, n+1, \gamma)$ is the logarithmic solution of the Kummer equation [37], given by

$$U(a, n+1, \gamma) = \frac{(-1)^{n+1}}{n!\Gamma(a-n)}[\Phi(a, n+1, \gamma)\ln\gamma$$

$$+ \sum_{r=0}^{\infty} \frac{(a)_r \gamma^r}{(n+1)_r r!}\{\psi(a+r) - \psi(1+r) - \psi(1+n+r)\}]$$

$$+ \sum_{1}^{n} \frac{(n-1)!}{\Gamma(a)}\gamma^{-n}\Phi(a-n, 1-n, \gamma) \ , \tag{A16}$$

where, $\Phi(a, n+1, \gamma)$ is the Kummer function of the first kind, $\Gamma(a)$ is the gamma function,

$$\psi(a) = \frac{\Gamma'(a)}{\Gamma(a)} \ , \tag{A17}$$

and

$$(a)_n = a(a+1)(a+2)...(a+n-1), (a)_0 = 1 \ . \tag{A18}$$

Since for $x = 0$, $\gamma = -2\alpha^{1/2}k_0x_0$ is a negative quantity, $\ln\gamma$ in (A16) contributes an imaginary part which gives rise to the resistive component of ς_f in (A15). For $\omega/\omega_{ci} \rightarrow 0$, $\beta \rightarrow 0$ so that $[\Gamma(a-n)]^{-1} \rightarrow 0$ and the resisitive loading disappears. For a fixed value of α, increasing ω/ω_{ci} causes a rapid increase in β due to the increasing k_0 and $(x_0 - x_{c1})$. This in turn, causes a steep rise in the loading resistance as $[\Gamma(a-n)]^{-1}$ as well as $\Phi(a, n+1, \gamma)$ increase. The net result is a marked improvement in the conversion efficiency leading to the superior coupling properties at larger values of ω/ω_{ci} and hence at the higher toroidal wave numbers.

REFRENCES

[1]. ALFVÉN, H., Arkiv. Mat. Astron. Fysik **29B**(1942)2.

[2]. WINTERBERG, F., Ann. Phys. **25**(1963)174; Z. Naturforsch. **18a**(1963)701; Ann. Phys. **29**(1964)259; Ann. Phys. **32**(1965)348; Z. Naturforsch. **21a**(1966)1270.

[3]. DOLGOPOLOV, V. V., STEPANOV, K. N., Nucl. Fusion **5**(1965)276.

[4]. GROSSMAN, W., TATARONIS, J.A., Z. Phys. **261**(1973)217.

[5]. JANKOVICH, Z., in Proceedings of the Sixth European Conference on Controlled Fusion and Plasma Physics (Joint Institute for Nuclear Research, Moscow, 1973), Vol. 1, p. 621.

[6]. HASEGAWA, A., CHEN, L., Phys. Rev. Lett. **32**(1974)454; Phys. Rev. Lett. **35**(1975)370; Phys. Fluids **19**(1976)1924.

[7]. CHEN, L., HASEGAWA, A., Phys Fluids **17**(1974)1399.

[8]. TATARONIS, J. A., J. Plasma Phys. **13**(1975)87.

[9]. TATARONIS, J. A., GROSSMAN, W., Nucl. Fusion **16**(1976)667.

[10]. KAPRAFF, J. M., TATARONIS, J. A., J. Plasma Phys. **18**(1977)209.

[11]. OTT, E., WERSINGER, J.-M., BONOLI, P. T., Phys Fluids **21**(1978)2306.

[12]. KARNEY, C. F. F., PERKINS, F. W., SUN, Y.C., Phys. Rev. Lett. **42**(1979)1621.

[13]. STIX, T. H., in Heating in Toroidal Plasmas (Proc. 2nd Joint Varenna-Grenoble Int. Sym. Como, 1980), CEC, Brussels, Vol. II (1981)631.

[14]. APPERT, K., BALET, B., GRUBER, R., TROYON, F., TSUNEMATSU, T., VACLAVIK, J., ibid, 643; APPERT, K., BALET, B., GRUBER, R., TROYON, F., VACLAVIK, J., in Plasma Physics and Controlled Nuclear Fusion Research, 1980 (Proc. 8th Int. Conf. Brussels, 1980), Vol. 2, IAEA, Vienna (1981)43; KELLER, R., BUGMANN, G., CHEETHAM, A., HEYM, M., HOFMANN, F., LIETTI, A., LISTER, J. B., POCHELON, A., TUSZEL, A., in Radio-Frequency Plasma Heating (Proc. 4th Top. Conf. Austin, 1981)B2; APPERT, K., BALET, B., GRUBER, R., TROYON, F., TSUNEMATSU, T., VACLAVIK, J., Nucl. Fusion **22**(1982)903.

[15]. PURI, S., in Plasma Physics and Controlled Nuclear Fusion Research 1980 (Proc. 8th Int. Conf. Brussels, 1980), IAEA, Vienna (1981)51.

[16]. APPERT, K., GRUBER, R., TROYON, F., VACLAVIK, J., Plasma Phys. **24**(1982)1147.

[17]. ROSS, D.W., CHEN, G.L., MAHAJAN, S. M., Phys. Fluids **25**(1982)652.

[18]. CHAMBRIER, A. D., CHEETHAM, A. D., HEYM, A., HOFMANN, F., JOYE, B., KELLER, R., LIETTI, A., LISTER, J. B., POCHELON, A., Plasma Phys. **24**(1982)893.

[19]. MAHAJAN, S. M., ROSS, D.W., CHEN, G.L., Phys. Fluids **26**(1983)2195.

[20]. APPERT, K., VACLAVIK, J., Plasma Phys. **25**(1983)551.

[21]. STIX, T. H., SWANSON. D. G., in Handbook of Plasma Physics (GALEEV, A. A., SUDAN, R. N., Eds), North Holland, New York, 1983.

[22]. BERNSTEIN, I., Phys. Fluids **26**(1983)730.

[23]. HOFMANN, F., APPERT, K., VILLARD, L., Nucl. Fusion **24**(1984)1679.

[24]. MAHAJAN, S. M., Phys. Fluids **27**(1984)2238.

[25]. APPERT, K., COLLINS, G. A., HOFMANN, F., KELLER, R., LIETTI, A., LISTER, J. B., POCHELON, A., VILLARD, L., Phys. Rev. Lett. **54**(1985)1671.

[26]. BRUNEL, F., LEBOEUF, J.-N., MAHAJAN, S. M., Phys. Rev. Lett. **54**(1985)1252.

[27]. PURI, S., in Course and Workshop on Applications of RF Waves to Tokamak Plasmas(Proc. International School of Plasma Physics "Piero Caldirola", Varenna, 1985) Vol. II, (1985)817.

[28]. ROSS, D. W., YANMING, L., MAHAJAN, S. M., MICHIE, R. B., Nucl. Fusion **26**(1986)139.

[29]. RIYOPOULOS, S., MAHAJAN, S. M., Phys. Fluids **29**(1986)731.

[30]. COLLINS, G. A., HOFMANN, F., JOYE, B., KELLER, R., LIETTI, A., LISTER, J. B., POCHELON, A., Phys. Fluids **29**(1986) 2260.

[31]. PURI, S., Nucl. Fusion (to be published).

[32]. STIX, T. H., in The Theory of Plasma Waves, McGraw-Hill, New York, (1962).

[33]. FRIED, B. D., CONTE, S. D., in The Plasma Dispersion Function, Academic, New York, 1961.

[34]. PURI, S., Phys. Fluids **27**(1984)2156.

[35]. STRANG, G., FIX, G.J., in An Analysis of the Finite Element Method, Prentice-Hall, New Jersey, 1973.

[36]. BERS, A., JACQUINOT, J., LISTER, G., in Heating in Toroidal Plasmas (Proc. 2nd Joint Varenna-Grenoble Int. Sym. Como, 1980), CEC, Brussels, Vol. I (1981)569.

[37]. SLATER, L. J., in Handbook of Mathmatical Functions with Formulas Graphs and Mathematical Tables (ABRAMOWITZ, M., STEGUN, I. A., Eds), National Bureau of Standards, U. S. Department of Commerce, Washington D. C., 1964.

TABLE I

r_T	*toroidal radius*	1.65 m
r_p	*poloidal radius*	0.5 m
B_0	*toroidal magnetic field*	3.0 T
$n_e(0)$	*peak density on axis*	$3 \times 10^{20}\ m^{-3}$
$n_e(r_p)/n_e(0)$	*relative edge density*	0.01
χ_n	*density profile weight*	2
σ_n	*density profile variance*	4
$T_e(0)$	*peak electron temperature*	7 keV
$T_e(r_p)/T_e(0)$	*relative edge temperature*	0.01
χ_t	*temperature profile weight*	2
σ_t	*temperature profile variance*	4
q_{min}	*safety factor on axis*	1
q_{max}	*safety factor at edge*	3
χ_q	*q profile weight*	2
σ_q	*q profile variance*	4
r_A/r_p	*resonance position*	0.67
N	*antenna toroidal number*	8
2ℓ	*antenna length*	0.8 m
$2w$	*antenna width*	0.15 m
$2b$	*antenna wall sparation*	0.15 m
	gas composition	H_2

TABLE I ASDEX UPGRADE PARAMETERS USED IN THE COMPUTATIONS

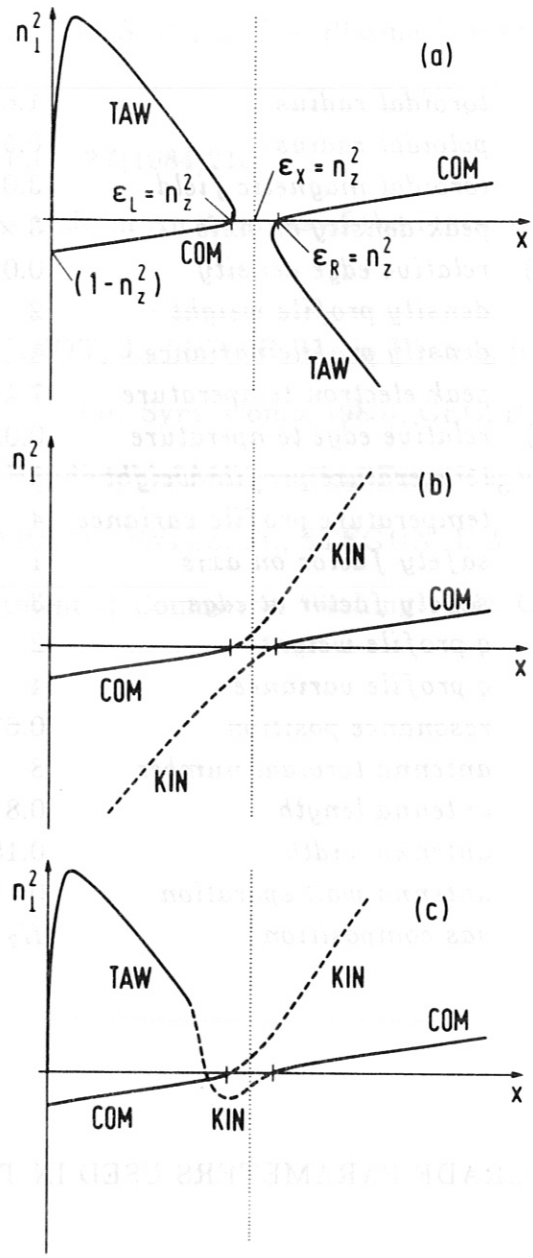

Fig. 1 The qualitative Alfvén wave dispersion curves for (a) a cold plasma, (b) a hot plasma, and (c) a plasma with an increasing temperature in the direction of the density gradient. The left and the right cutoffs occur at $\epsilon_{L,R} = n_z^2$ and the position of the Alfvén layer is given by $\epsilon_x = n_z^2$. The dashed parts of the dispersion curves correspond to the regions with significant Landau damping. In the limit of vanishing electron mass both TAW and KIN collapse to form a vertical branch at the Alfvén singularity.

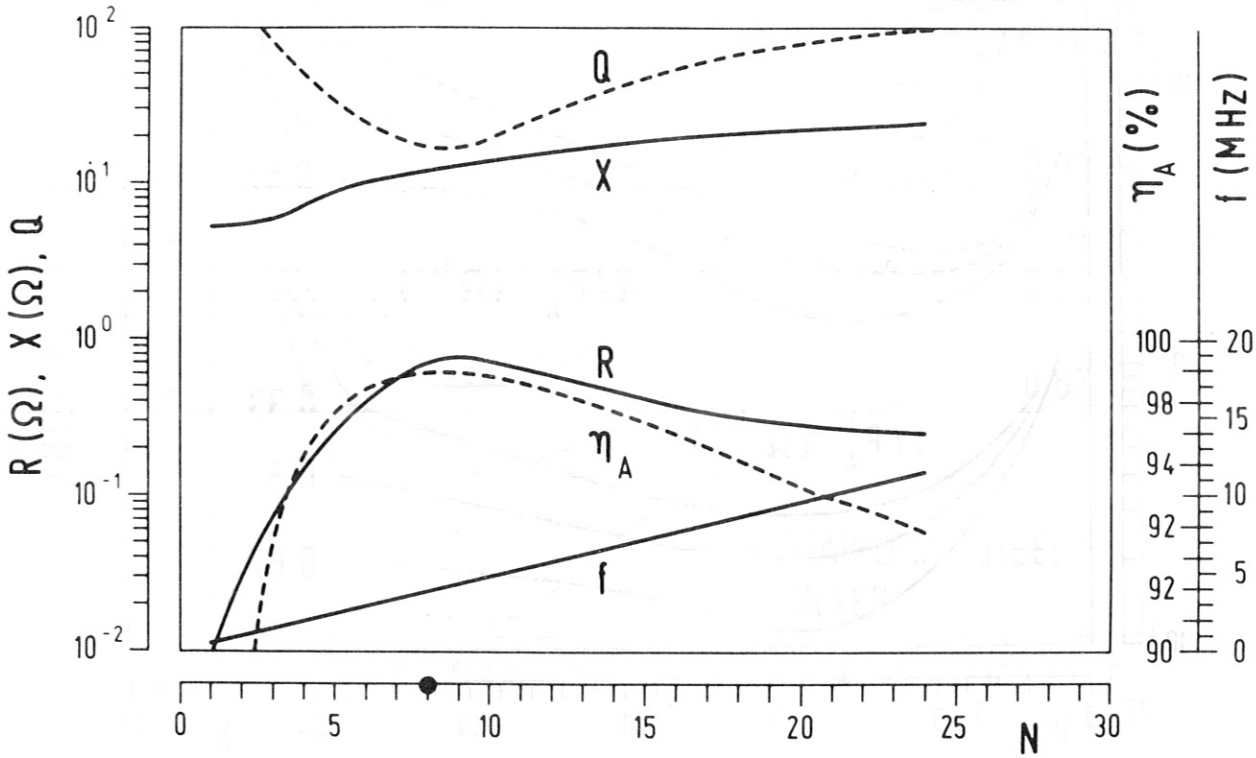

Fig. 2 Dependence of antenna loading on the toroidal number N. Antenna loading falls sharply below $N \sim 5$, much as in the absence of the plasma equilibrium current.

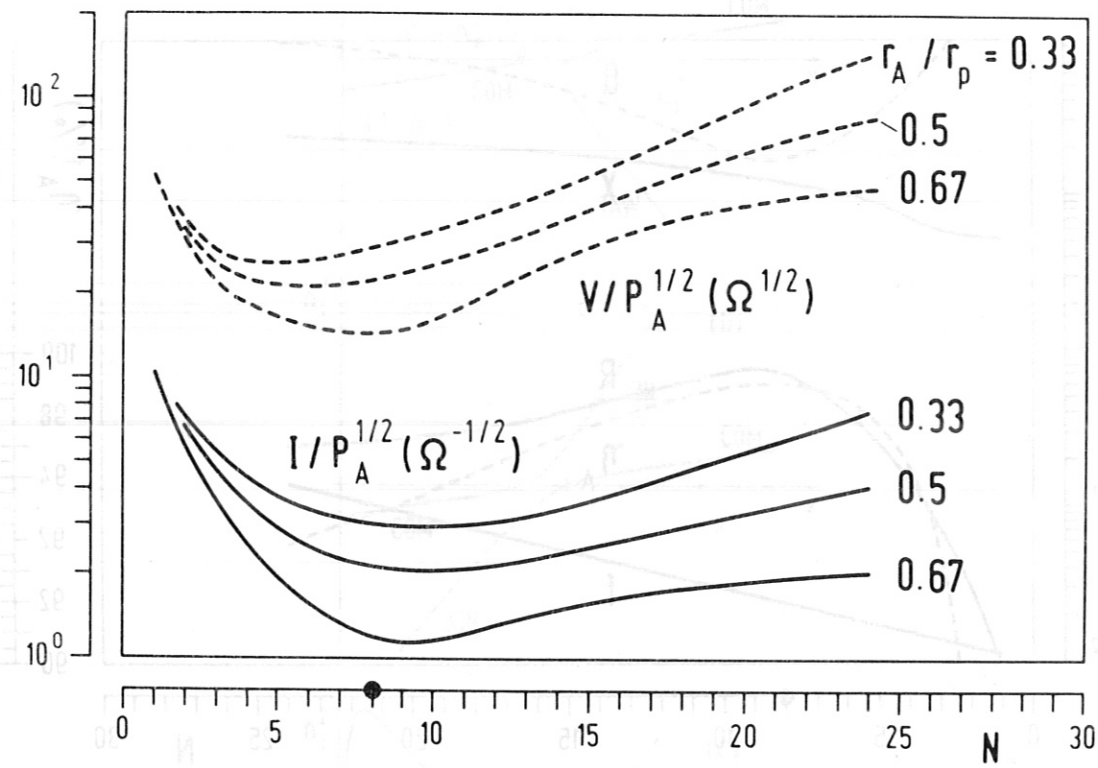

Fig. 3 The antenna voltage and current characteristics as a function of the input power P_A and the resonance position r_A/r_p versus N.

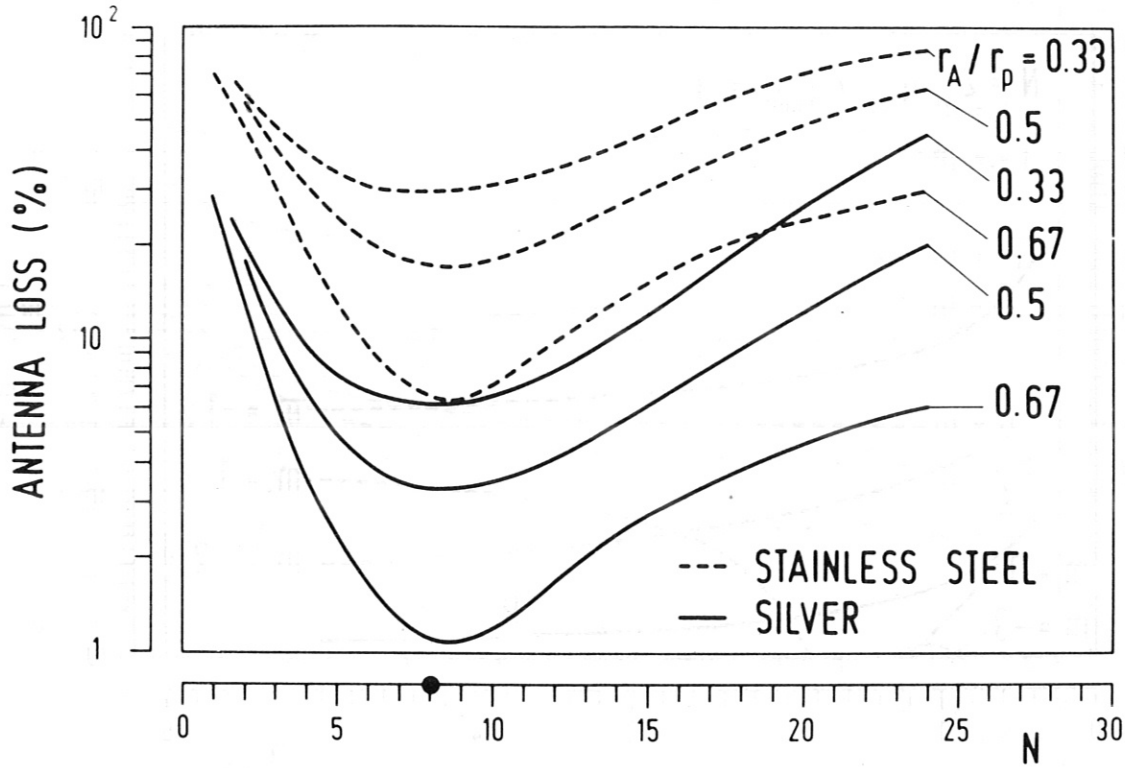

Fig. 4 Antenna resistive loss for the case of stainless steel and silver plated antennas, respectively. The large voltage and current requirements as well as the high losses associated with the low N values would preclude their use in thermonuclear applications.

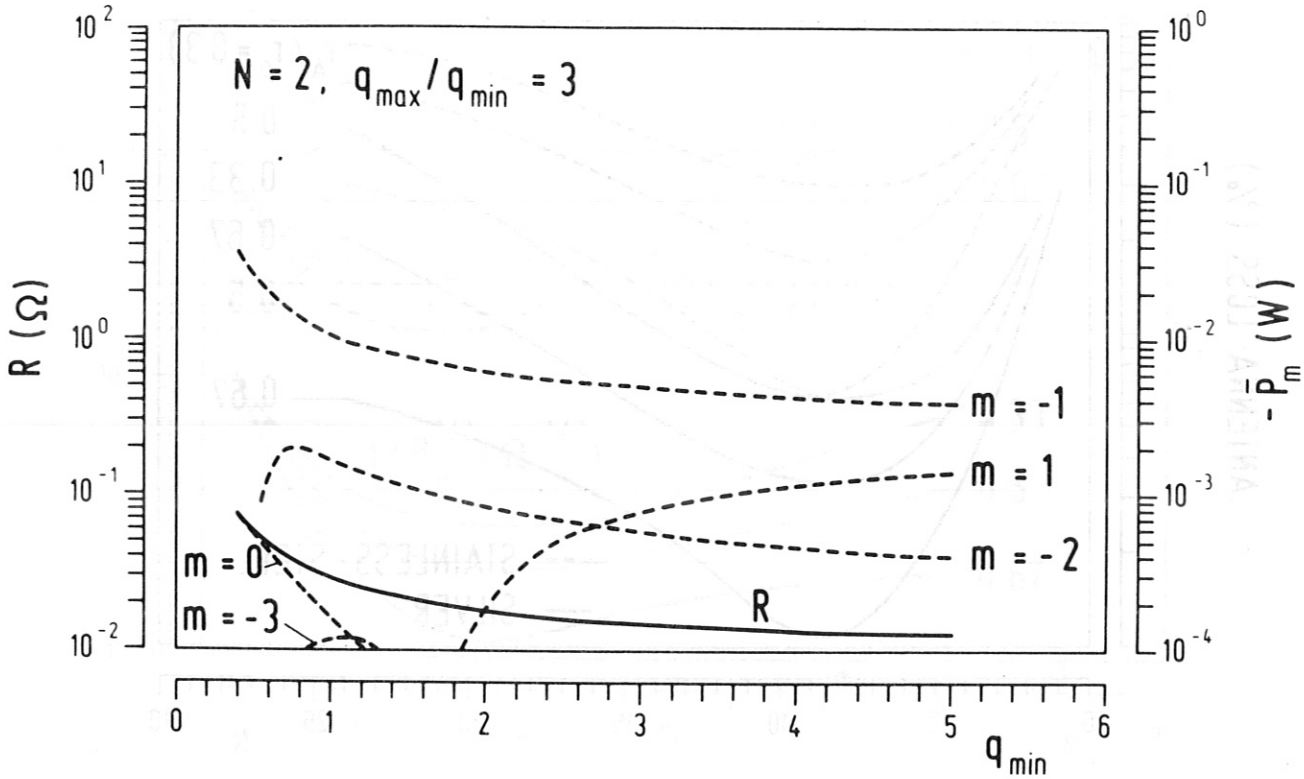

Fig. 5 Improvement in antenna loading with the plasma equilibrium current for $N = 2$ by a factor of approximately 2.5. The loading, however, is still too low to be viable for thermonuclear applications. Notice the clear distinction in the loading characteristics for the the positive and the negative azimuthal numbers.

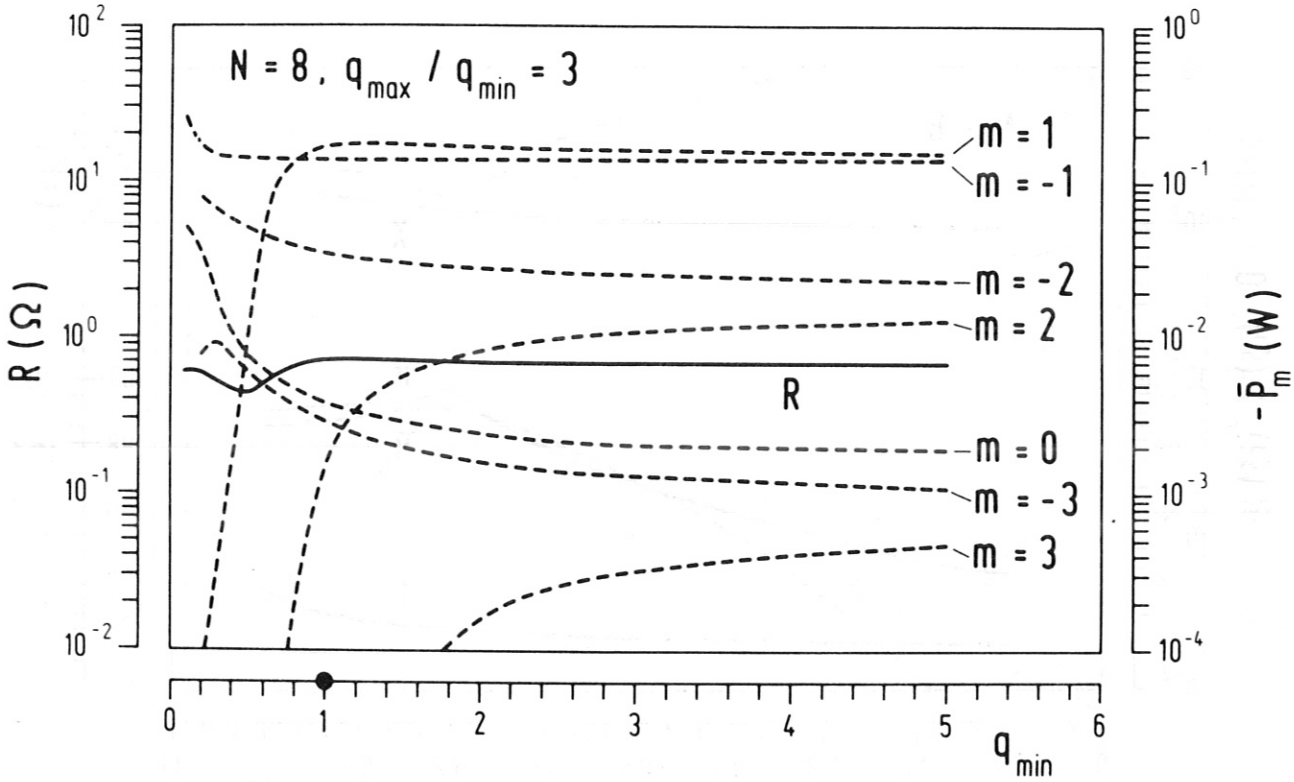

Fig. 6 The plasma current produces insignificant changes in the antenna loading for the large $N = 8$ antenna configuration.

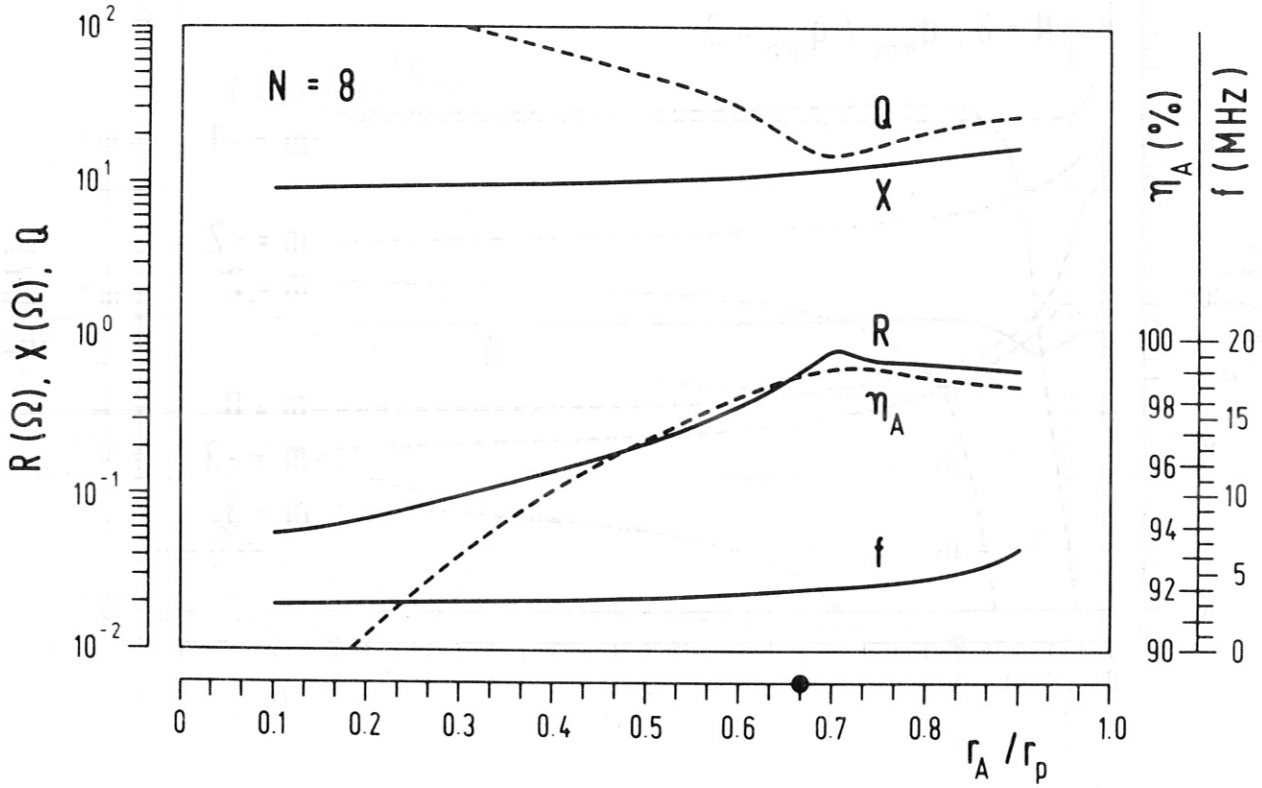

Fig. 7 Antenna loading as a function of the resonance position r_A/r_p for $N = 8$. The rapid reduction in coupling as the resonance moves deeper in the plasma is due to the strong radial evanescence for the closely spaced antenna configuration.

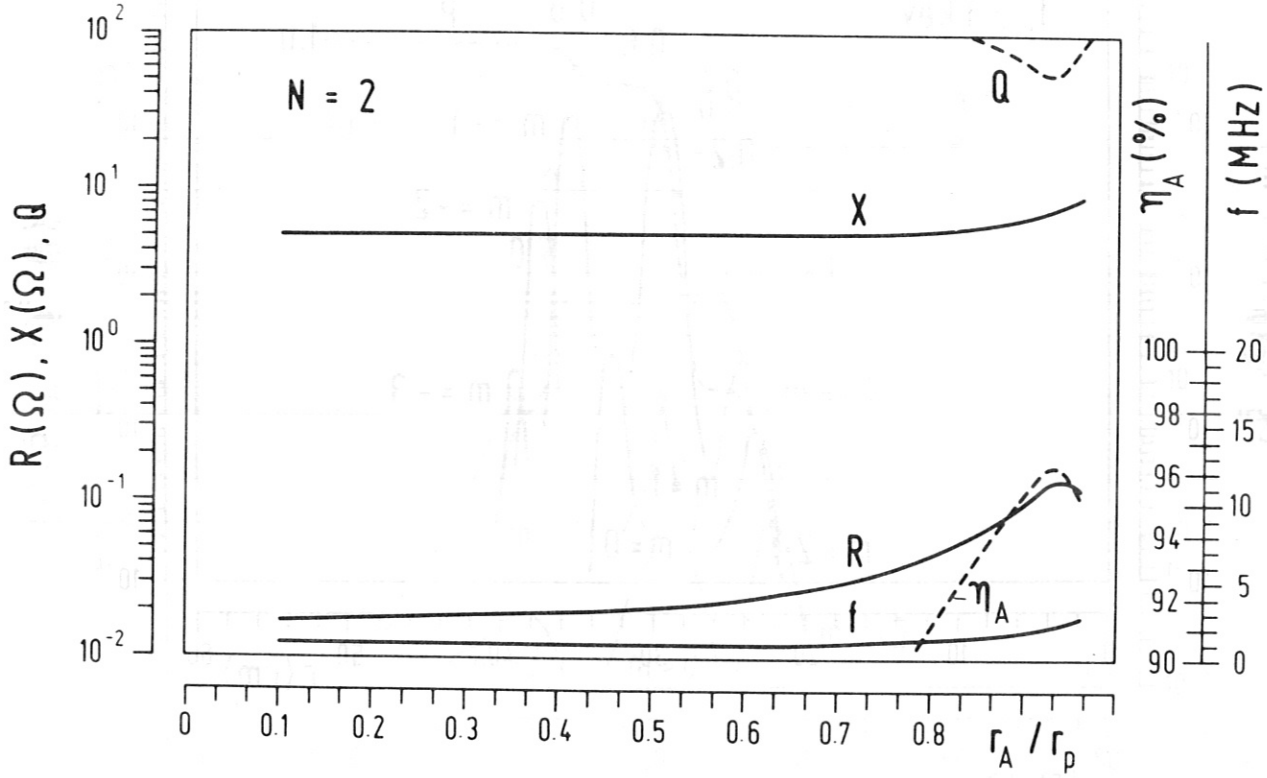

Fig. 8 The loading for the $N = 2$ antenna configuration exhibits less sensitivity to the resonance position but remains uniformly low.

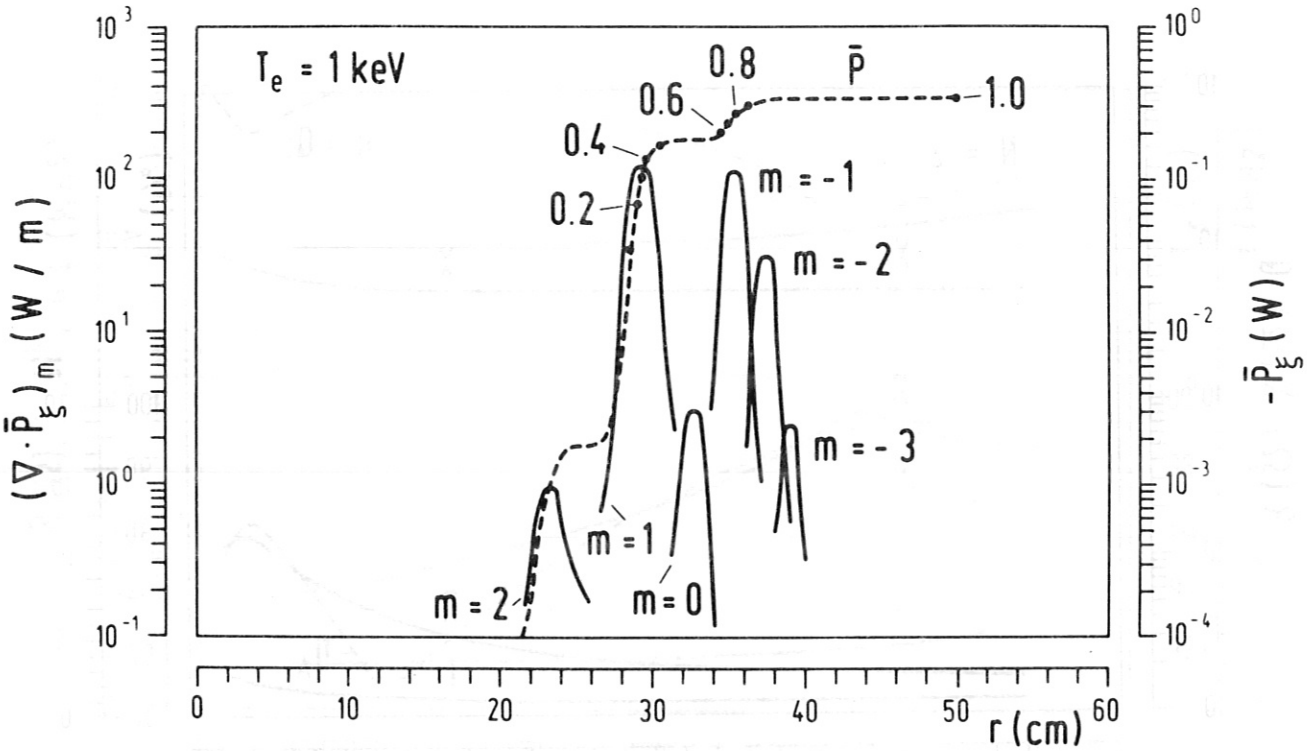

Fig. 9 $-\bar{\mathbf{P}}_\xi$ (dashed curve; the dots indicate the fraction of the wave energy already absorbed) and $(\nabla \cdot \bar{\mathbf{P}})_m$ (solid curves) for $T_e = 1\ keV$. The differing locations of the resonance for the different m in conjunction with the finite temperature effects considerably broadens the absorption profile. Since most of the dissipation occurs in the $m = \pm 1$ azimuthal modes, this advantage will not be present for the low mode numbers where the coupling to the $m = +1$ is effectively suppressed.

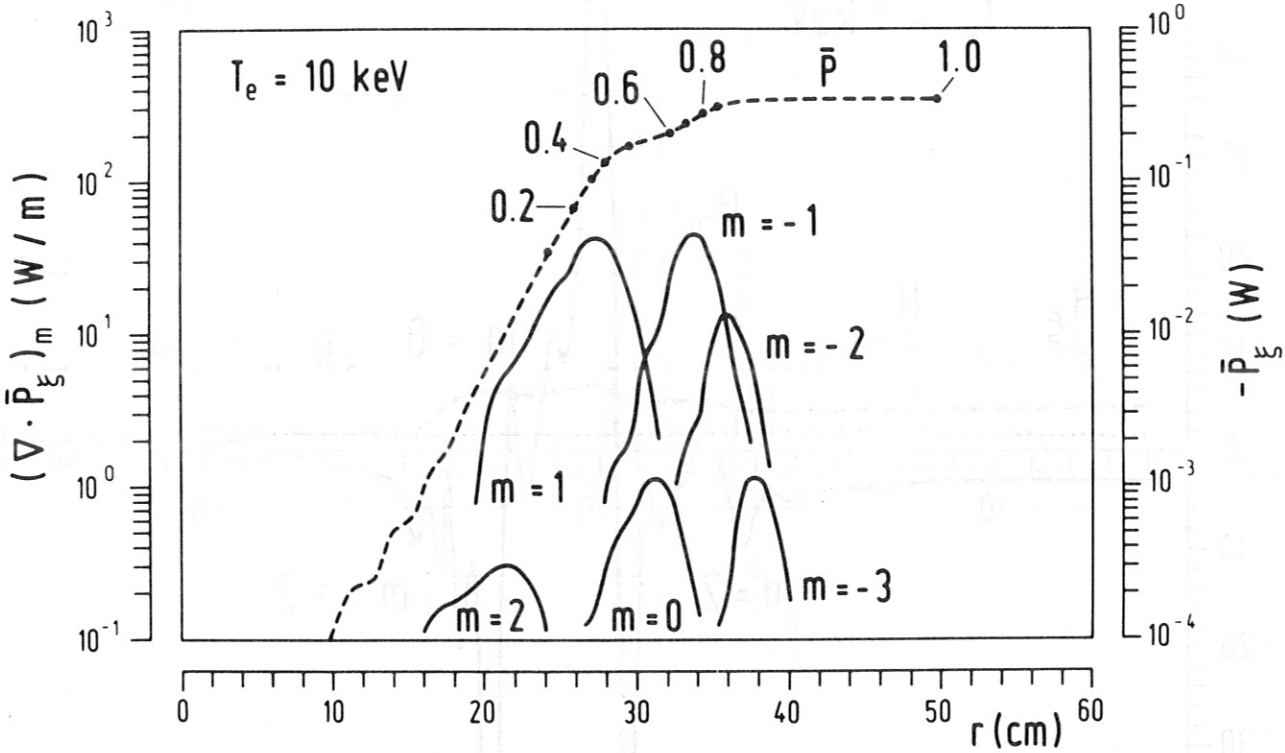

Fig. 10 $-\bar{\mathbf{P}}_\xi$ and $(\nabla \cdot \bar{\mathbf{P}})_m$ for $T_e = 10\ keV$.

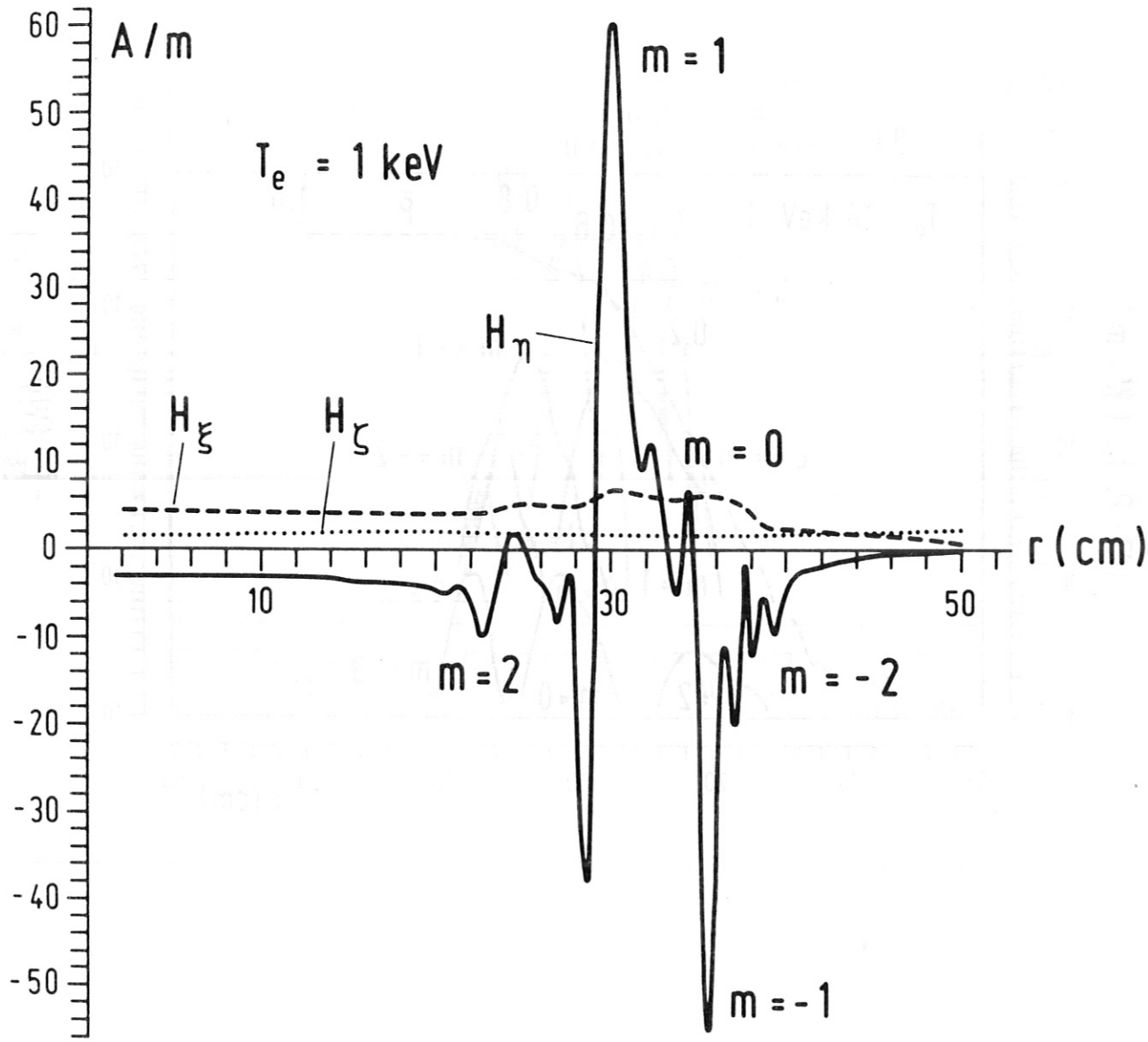

Fig. 11 The magnetic field components in the plasma for the reference parameters. The large excursions in H_η compensate for the low values of E_ς in order to provide the requisite conditions for the transport of the wave converted energy.

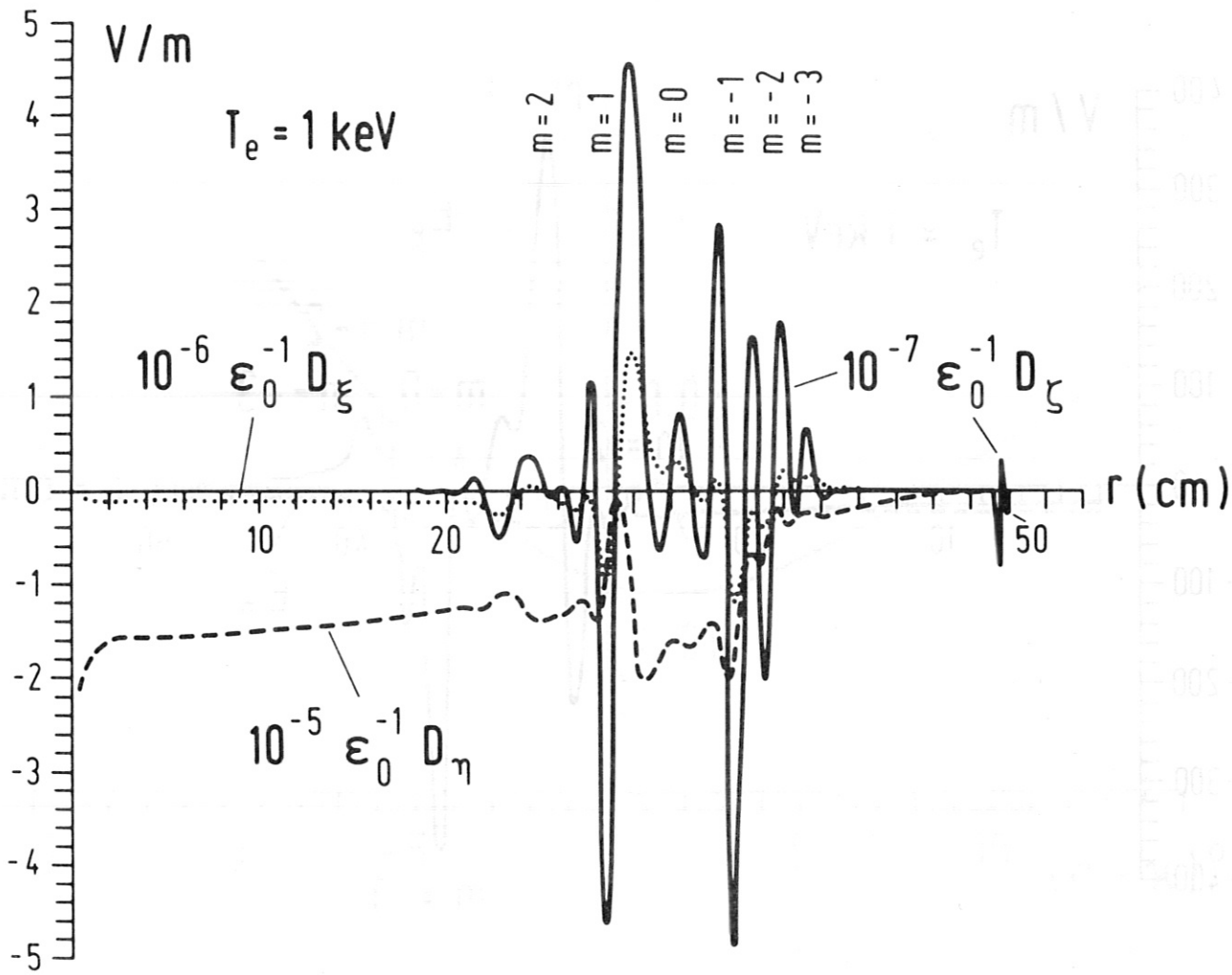

Fig. 12 Components of the displacement vector $\mathbf{D} = \epsilon \cdot \mathbf{E}$. The component D_ζ increases near the resonances to provide for the E_ζ needed for carrying the slow wave energy. D_ξ follows the D_ζ variations in order to satisfy the continuity condition for $\mathbf{D}$.

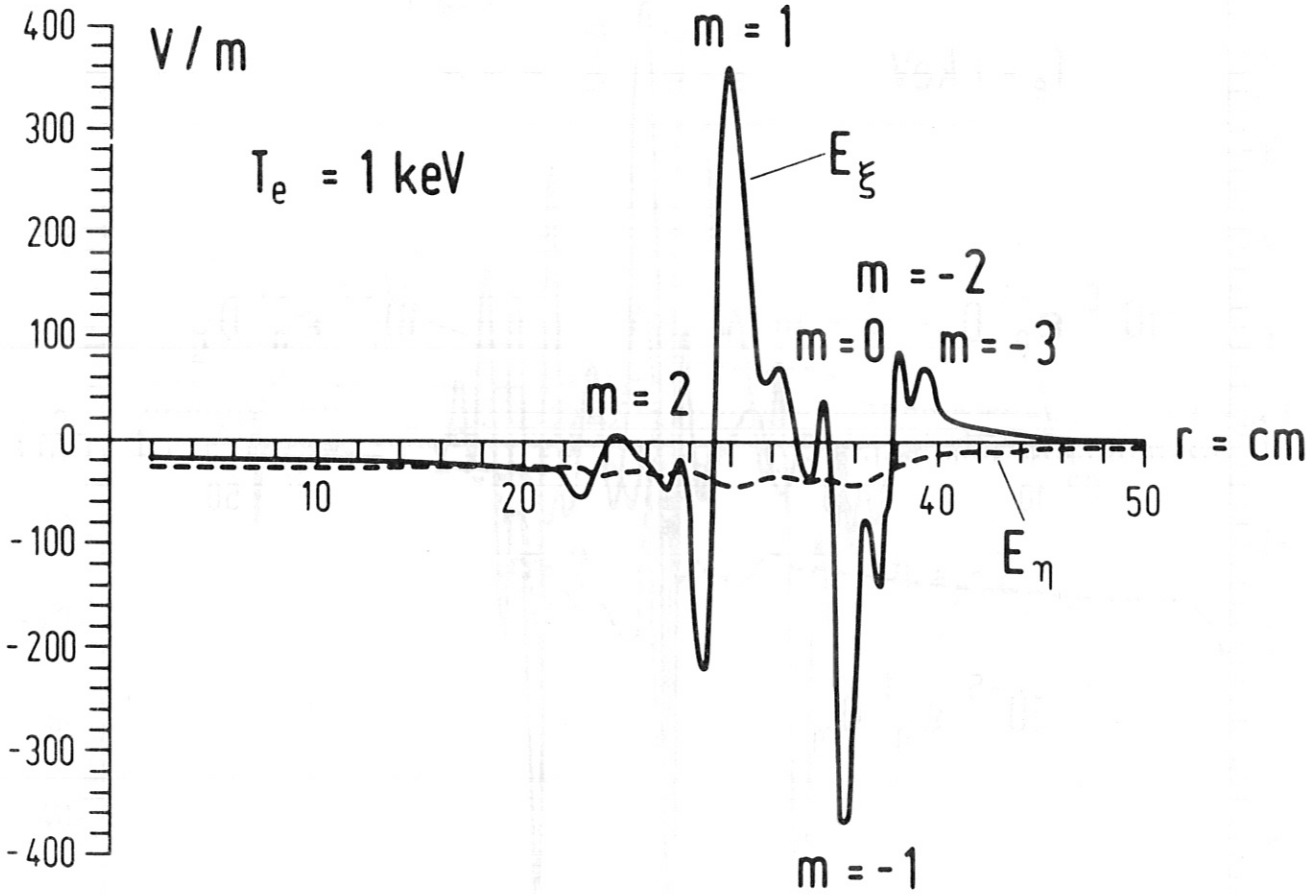

Fig. 13 The electric field in the plasma. The E_ς component, being several orders of magnitude smaller, is not shown.

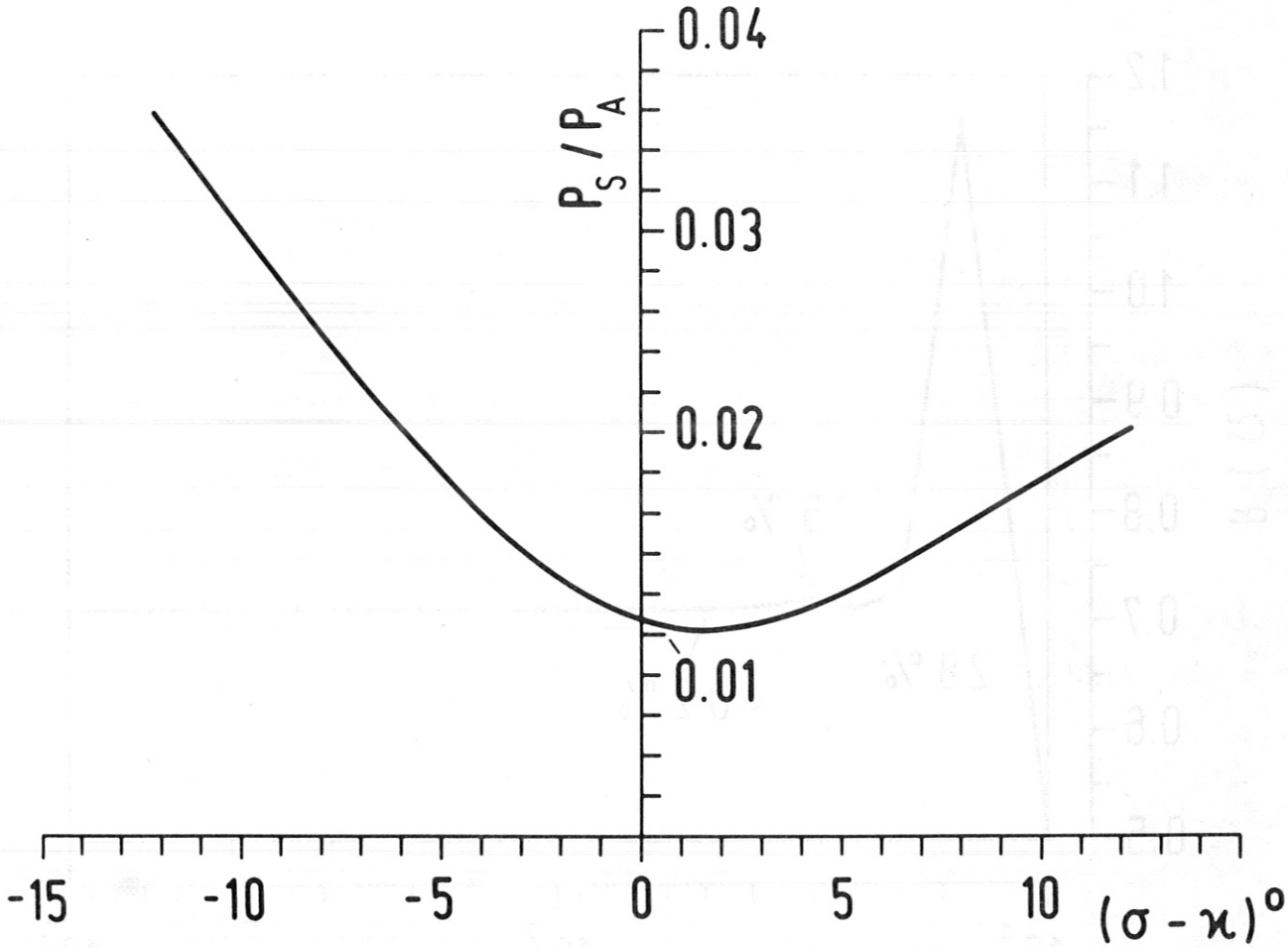

Fig. 14 Fraction of the antenna energy coupled to the surface wave as a function of the angle $(\sigma - \chi)^\circ$ of the Faraday shield with the direction of the magnetic field lines.

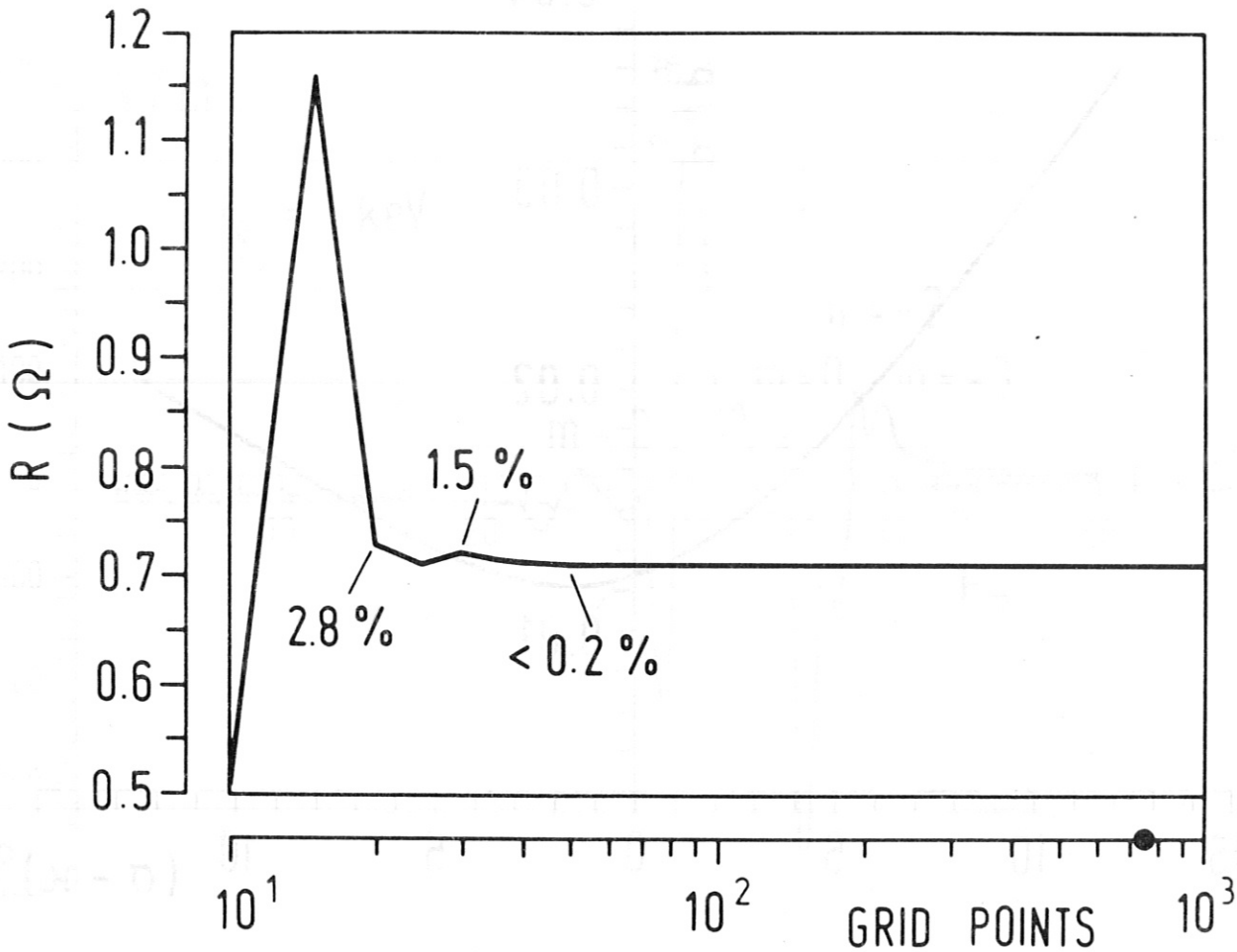

Fig. 15 Convergence of the antenna loading resistance versus the number of the radial grid points in the finite element integration of (43). Convergence within 0.2% of the final value occurs already for a scant 50 grid points. The computations reported in this paper employ 750 grid points throughout.